Aircraft Design and Testing of FLEXOP Unmanned Flying Demonstrator to Test Load Alleviation and Flutter Suppression of High Aspect Ratio Flexible Wings

Roessler, Christian; Stahl, Philipp; Sendner, Franz; Hermanutz, Andreas; Sodja, Jurij; De Breuker, Roeland; Koimtzoglou, Christos; Kotinis, Dimitrios; Georgopoulos, P.; More Authors

DOI
10.2514/6.2019-1813

Publication date
2019

Document Version
Final published version

Published in
AIAA Scitech 2019 Forum

AIAA SciTech Forum
7-11 January 2019, San Diego, California
AIAA Scitech 2019 Forum

10.2514/6.2019-1813

Aircraft Design and Testing of FLEXOP Unmanned Flying Demonstrator to Test Load Alleviation and Flutter Suppression of High Aspect Ratio Flexible Wings

Christian Roessler[1], Philipp Stahl[2], Franz Sendner[3], Andreas Hermanutz[4], Sebastian J. Koeberle[5], Julius Bartasevicius[6], Vladyslav Rozov[7], Christian Breitsamter[8], Mirko Hornung[9]
Technical University of Munich, Boltzmannstraße 15, Garching/München, 85748, Germany

Yasser M. Meddaikar[10], Johannes K. S. Dillinger[11]
German Aerospace Center DLR-Institute of Aeroelasticity, Göttingen, Lower Saxony, 37073, Germany

Jurij Sodja[12], Roeland de Breuker[13]
Delft University of Technology, Delft, South-Holland, 2629HS, The Netherlands

Dr. Christos Koimtzoglou[14], Dimitrios Kotinis[15], Panagiotis Georgopoulos[16]
INASCO Hellas Co, 18 Napoleontos Zerva str, Glyfada, Athens, 16675, Greece

The idea of the EU funded FLEXOP project is to raise efficiency of a currently existing wing by derivative solution with higher aspect ratio at no excess structural weight. In order to enable such a resulting highly flexible wing the project goal is to develop methods for active suppression of flutter and passive load alleviation. The developed methods will be tested and validated with a UAV flutter demonstrator. The demonstrator is a 7m wingspan, 65kg MTOW UAV equipped with a jet engine. After ground testing, including static load and ground vibration tests the demonstrator will be flown within VLOS with three different sets of wings: One baseline rigid wing, one wing tailored for passive load alleviation and one very flexible wing to test active flutter control. The paper describes the design methods of the demonstrator and gives an overview about the planned tests on ground and in flight to validate the flutter prediction models. A special emphasis is on in flight wing shape measurement with an installed fiber brag system.

[1] Research Associate, Institute of Aircraft Design
[2] Research Scientist Institute of Aircraft Design
[3] Research Scientist, Institute of Aircraft Design
[4] Research Scientist, Institute of Aircraft Design
[5] Research Scientist, Institute of Aircraft Design
[6] Research Scientist, Institute of Aircraft Design
[7] Research Scientist, Chair of Aerodynamics and Fluid Mechanics
[8] Professor, Chair of Aerodynamics and Fluid Mechanics, AIAA Associate Fellow
[9] Professor, Head of the Institute of Aircraft Design
[10] Research Scientist, Loads Analysis and Aeroelastic Design
[11] Research Scientist, Loads Analysis and Aeroelastic Design
[12] Senior Scientist, Faculty of Aerospace Engineering, Aerospace Structures and Computational Mechanics, AIAA member
[13] Associate Professor, Faculty of Aerospace Engineering, Aerospace Structures and Computational Mechanics, AIAA member
[14] Managing Director
[15] Aerospace Engineer
[16] Aerospace Engineer

I. Introduction

Flutter Free **FL**ight **E**nvelope e**X**pansion for ec**O**nomic **P**erformance improvement (FLEXOP) is a project within the European Union's Horizon 2020 framework. Its main goal is to raise efficiency of a currently existing wing by derivative solution with higher aspect ratio at no excess structural weight. The benefit of increased span will be increased lift to drag ratio and therefore less fuel burn. This should be accomplished ideally with no mass penalty. The downside of the more slender lightweight wings is their higher flexibility which arises the problems of aeroelasticity. Especially flutter speed will be lower than for a more rigid wing. Therefore very accurate methods for flexible mode modelling and robust flutter control synthesis should be developed within FLEXOP with the aim to fly at the same speed as the baseline aircraft with the enabling features of active flutter control and passive load alleviation to reduce the increased loads on higher aspect ratio wings. The developed methods will be validated with a UAV flutter demonstrator. The 7m span, 65 kg TOW demonstrator will feature three different set of wings: One baseline rigid wing, one wing tailored for passive load alleviation and one very flexible wing to test active flutter control. After validating the methods and tools the potential of those technologies should be evaluated within a scale up study. Over Airbus XRF1 reference aircraft model, the potential of either 20% payload increase or 7% improvement in fuel efficiency is expected [1].

Figure 1: FLEXOP Demonstrator UAV [2]

To design a safe and performant aircraft with flexible wing technology, the design-driving aeroelastic behavior has to be considered with high fidelity already at early design stages. Validated and precise methods are required to model an aircraft's aeroelastic characteristics which need to be arranged in the right order for the aircraft design process. This process is described in the next chapter for the design of the demonstrator with a very flexible flutter test wing. After designing the flutter test wing the methods for deriving a wing for passive load alleviation together with a conventional rigid baseline wing are shown. In the second part of the paper the ground and flight tests are explained. The ground tests comprise of static tests for validating the stiffness matrices of the models and ground vibration testing for validating the eigenmodes and frequencies. The flight tests should prove the active flutter suppression methods as well as the passive load alleviation wing. For in flight wing shape and load measurements the demonstrator is equipped with a fiber brag system. This system is described in the last part of this paper.

While this paper focuses on the demonstrator design and testing within the Flexop project, it has been presented together with papers on aeroservoelastic modeling [3] and controller development [4] of the Flexop UAV, along with work [5-7] on the Performance Adaptive Aeroelastic Wing (PAAW) project in a joint Flexop-PAAW session.

II. FLEXOP Demonstrator UAV Design

A. Flutter Wing Aircraft Design Process

1. Demonstrator Requirements

The main purpose of the demonstrator is to test and validate the developed methods for load alleviation, flutter prediction and flutter controller design. The shape of the wing should thereby be similar to a next generation airliner. The test flights should take place in Germany. Due to law restrictions it is only possible to fly within line of sight [8] which gives limitations to the maximum test speeds [9]. This implies special requirements for the propulsion system. As the turns should be flown with a safe speed below flutter test speed the aircraft must be capable of fast acceleration and deceleration.

Following requirements that are important to understand the design outcome are summarized.

- A conventional dragon configuration shall be used. The wing planform shall resemble the one of a large new generation transportation aircraft.
- A measurement payload of around 2kg has to be carried.
- Due to logistic restrictions the maximum part size of the unrigged aircraft must not exceed 4 m.
- Unassisted taxi, takeoff and landing on the ground shall be possible
- The landing approach has to be possible at a glide path of 1/7 or steeper
- The time, the aircraft has to stay at target speed should not be less than 10 seconds. The time to settle the targeted airspeed without severe overshoot, the time for excitation and the time to record the structures oscillation have to be minimized

A preliminary analyses showed that an aircraft able to achieve the intended mission is feasible if a sufficient low flutter speed not greater than 57 m/s is achievable [9]. Nevertheless the acceleration and deceleration mission segments demand propulsion and breaking systems with short response times. The timespan the aircraft needs for acceleration and deceleration however is in the magnitude of some propulsion and airbrake systems' response times. A representation of the affected systems' dynamics as well as a mission simulation with short time step is therefore required.

2. *Design Process*

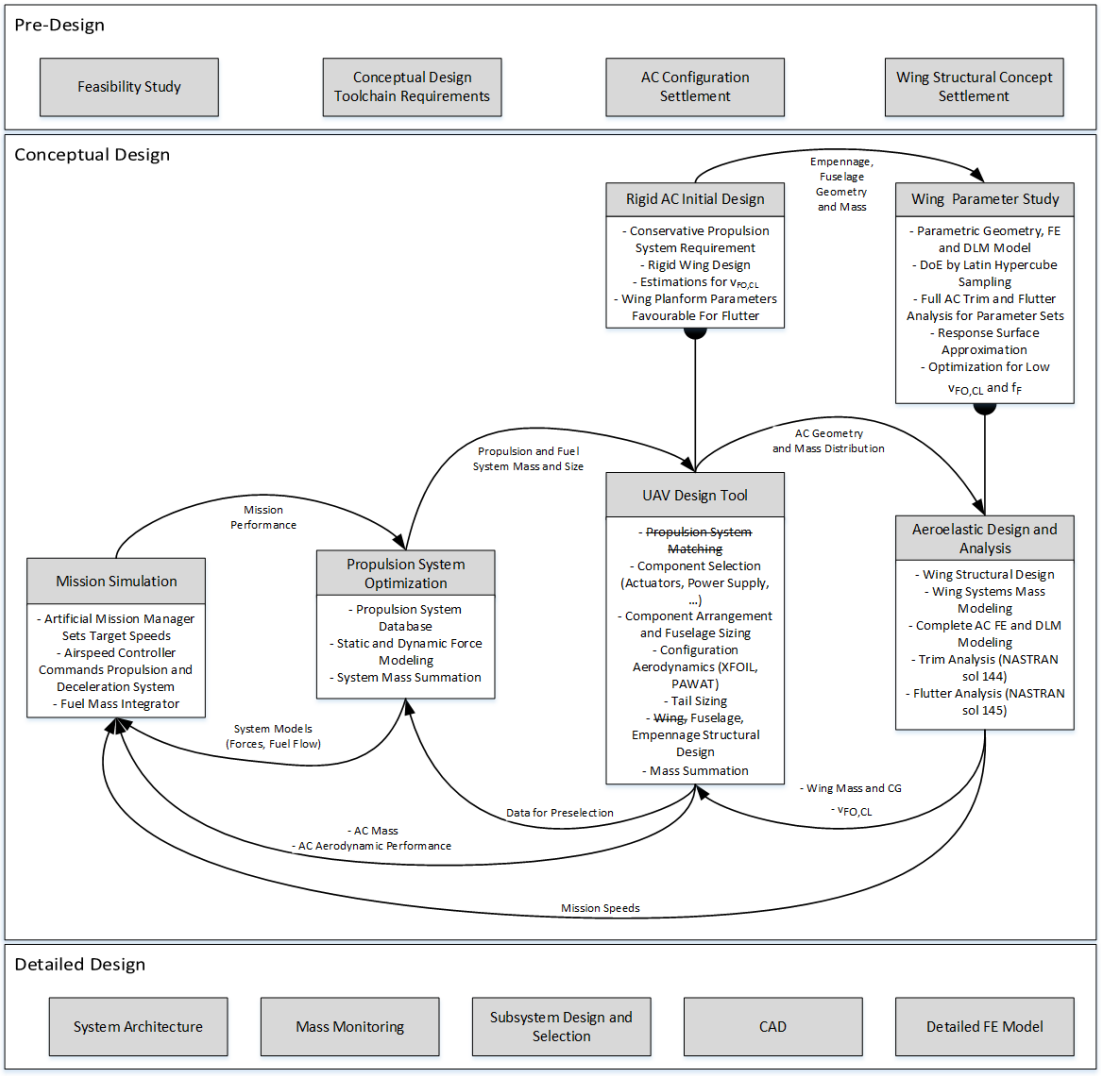

Figure 2: Workflow of the flexible wing aircraft design process used for the FLEXOP demonstrator [9]

The most critical wing to design is the flutter test wing because low flutter onset speed as well as low flutter frequency due to actuator limitations are required. This requires a very flexible wing but on the other hand the

wing has to withstand maneuver loads during flight testing. Furthermore the divergence speed has to be considerably higher than the flutter onset speed in order to operate the demonstrator safely. Therefore the aircraft design process was tailored to the flexible wing with the goal to find a parameter set that fulfills all mission requirements and features low mass and size as this typically directly affects operability and costs. An overview of the aircraft design process established by the Institute of Aircraft Design at the Technical University of Munich is given in Figure 2 [9].

In the initial **Pre-Design** phase a feasibility study has been done, toolchain requirements have been set and an aircraft configuration and wing structural concept have been found.

At the beginning of the **Conceptual Design**, an existing **UAV Design Tool** [11] was used to design an aircraft with a classic rigid wing to serve as starting point. The in-house design tool for electrically driven propeller UAV was extended for the additional use of reciprocating and jet engines. Besides the propulsion system selection, the tool incorporates aircraft systems, aerodynamics, mass estimation and sizing modules. With the aerodynamics module, the aircraft can be trimmed and drag polars can be calculated as needed for propulsion system selection and performance calculations. The module also includes the determination of the maximum lift coefficient and thus stall speed. Here, airfoil polars are calculated with XFOIL while an extended lifting line theory is used on wing level. In the mass estimation module, the structure of the aircraft components is analytically sized by both strength and maximum allowed deformation. That enables the calculation of the masses of each component, which are subsequently added up to a total mass breakdown. In the sizing module, the empennage is sized to fulfil the flight mechanic stability requirements. Also the fuselage is shaped to fit all components and simultaneously achieve the desired center of gravity. On the propulsion system side, each subcomponent required for the chosen propulsion system type is selected by calculating performance parameters and matching of the components. The general philosophy is to select commercially available hardware components wherever possible. In that way, the time to realize a design as flying demonstrator is minimized. However, the biggest advantage is the use of reliable manufacturer data. Therefore, databases of commercially available components have been compiled and amended to fit the size class of the FLEXOP demonstrator UAV. To size the propulsion system, a static acceleration like in the feasibility study was requested at target speed. This approach could be implemented in the existing tool structure and is conservative. It became clear early in the design process that an electric propeller driven aircraft is not competitive to its reciprocating or jet engine alternatives due to the disadvantageous energy density of the batteries. The masses of the reciprocating and jet engine powertrain were comparable. Due to good integrability, a wide range of off-the-shelf options, good high speed performance and low vibration level, an affinity towards a jet engine solution was established. A detailed investigation on the question of the propulsion system however had to follow as the impact of the jet engine's slow throttle response was still unconsidered. By the variation of basic parameters like wing area, aspect ratio, sweep, taper ratio and wing airfoil, a mission-capable configuration could be identified within the desired parameter ranges. This configuration was the baseline to run a study on the wing's aeroelastic influence parameters.

This influence is investigated by a response surface approximation of the aeroelastic properties open loop flutter onset airspeed $v_{FO,OL}$ and flutter frequency at flutter onset f_{FO}. As design parameters, the wing surface, leading edge sweep, aspect ratio and taper ratio are used. On the structural side, the position of the main spar and spar cap width is included as parameters. With these parameters geometrical, structural and aerodynamic models for the wing are automatically generated. A wing Finite Element model, mostly consisting of shell elements, incorporates the composite layups and mass items from structure and aircraft systems. The composite layup in the wing skin is an unvaried sandwich construction with thinnest commercially available glass fiber (GFRP) laminates. To complete the structural full aircraft model, rigid fuselage and empennage are added. The Doublet Lattice Method (DLM) is used for steady and unsteady aerodynamic force modelling. Therefore, it is necessary to couple the panel mesh with the wing planform. For the parameter study, only aerodynamic forces at the wing and empennage are considered.

In total, the system is build up with six design variables, on which a numerical design of experiments is performed. The design of experiments construction points are chosen after the Latin Hypercube Sampling method. To get a mathematical description, the numerical results are assembled with the last square approximation method to a response surface of a quadratic polynomial order. With an oversampling of two, it is necessary to calculate and evaluate 62 design points within the chosen design space. To identify a convenient wing configuration on the response surface approximation, the objective is formulated as an optimization task. Therefore the objective function is defined to fulfill the test flight mission task. Additional side constraints are used to filter out wing configurations violating safe aircraft operation. The optimization task can be stated as: minimize the flutter frequency with the side constraint of keeping the maximum flutter speed below 50 m/s. The study uses NASTRAN's solution 145 flutter calculation which is based on the *p-k* method. In addition, the maximum wing tip displacement in the 5g load case should be below 10% of the wing span and aileron reversal is prohibited below 60 m/s airspeed. The latter constraints are indirectly dependent on the wings bending and torsional stiffness and determined by a NASTRAN solution 144 static aeroelastic trim calculation.

The flutter onset velocity and first mode frequency are however too high to enable the planned mission. In a follow up study, the application of flutter tuning masses was investigated in the same manner of parameter variation and response surface approximation. The flutter onset velocity and first mode frequency could be reduced to values that likely enable the planned mission.

Together with the rigid aircraft initial design, the presented aeroelastic wing parameter study serves as input for the actual design iterations (see Figure 2). Four tool blocks are involved. The core is the known **UAV Design Tool**. The data of the structural wing design is, other than before, taken from the **Aeroelastic Design and Analysis Block**. As well, the airspeed of flutter onset is taken from there to structurally size the empennage. The aeroelastic block, in turn, uses the full aircraft geometry and mass distribution, to create an aeroelastic representation of the complete aircraft. The iteration is performed until a sufficient precise mass convergence is achieved.

A second link exists between the UAV design tool and the **Propulsion and Deceleration System Optimization Block** [12]. The main objective in this design process is to find a propulsion system providing sufficient acceleration and deceleration. Jet, turbo prop and reciprocating engines are considered for the propulsion task, airbrakes, variable pitch props and jet engine thrust reverser for the deceleration task. Besides static thrust and drag, fuel consumption, system mass and the transient characteristics are implemented. Suitable dynamic models, both for propulsion and deceleration, were identified and calibrated. Data of off-the-shelf available units of the most promising principles serve as calibration basis. Each of the propulsion-deceleration system combinations is evaluated by a numeric **Mission Simulation**. This simulation contains a point mass representation of the aircraft, assessing horizontal and vertical forces equilibria every time step. Aerodynamics are represented by the rigid aircraft drag polar. The flight mission contains a climb segment, multiple test segments, as well as cruise, turn flights and approach. Thereby, an artificial mission manager is setting the target airspeeds which a speed controller is trying to follow by commanding the deceleration and propulsion system. Preparation and take off were not simulated but represented by a fixed amount of fuel burn. Solutions not meeting the visual line of sight or test speed criterion are eliminated.

3. Detailed Aerodynamic investigations

After both the wing design and the pre-sized structural components are available, the DLM data are compared with high-fidelity CFD-based results. Therefore, Euler computations are performed with the small-disturbance, frequency-domain solver AER-SDEu that is developed at the Chair of Aerodynamics and Fluid Mechanics of the Technical University of Munich. Using the linearized Euler equations, complex three-dimensional flows including effects due to the geometrical thickness are reproduced. Thus, higher level of detail of the configuration geometry can be captured accurately. This ensures a more precise determination of the flutter boundary over the flight envelope and is also beneficial for an accurate and reliable control design.

AER-SDEu computes unsteady aerodynamic loads due to harmonic modal oscillations of the aircraft structure around the reference shape. Thus, a database of generalized aerodynamic forces (GAFs) can be generated by means of the tool for the subsequent linear flutter analysis. Figure 3 shows the distribution of the real and imaginary part of the first harmonic of c_p due to the excitation of the first symmetric wing-bending mode at the reduced frequency of 0.2, that represents a typical output of a simulation run.

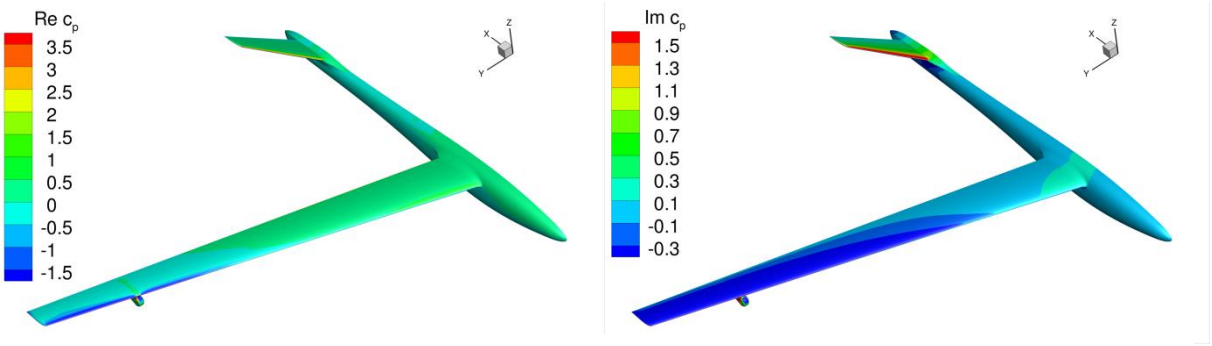

Figure 3: Contour plot of the real and imaginary part of the first harmonic of c_p due to the harmonic oscillation of the first symmetric wing-bending mode at $k_{red} = 0.2, Ma_\infty = 0.2, \alpha = -0.2°$.

On the one hand, the CFD grid representing the reference shape of the aircraft has to be provided as the input. On the other hand, also the CFD grids perturbed according to all considered modal deflections of the structure are required. They are derived from the reference CFD grid by means of the thin-plate-spline method and the transfinite interpolation. The shapes of structural modes are provided by the FEM modal analysis.

For the GAF-generation, a simulation run is performed at each reduced frequency for each considered Eigenmode. The GAFs at the reduced frequency of zero are used for the trim calculations both of the rigid and the aeroelastic

aircraft. In this way, the results of the flutter analysis as well as trim analysis based on computational methods of different fidelities can be juxtaposed.

4. Flutter Wing Demonstrator Results

Figure 4) features a very stiff composite manufactured fuselage, a low vibration 300N jet engine located on the fuselage back, combined with an airbrake system at the sides of the fuselage to enable fast deceleration, precise airspeed control and steep approach angles. The landing gear has two side by side retractable main gears together with small tail and wingtip wheels to enable unassisted ground taxi, takeoff and landing. The composite empennage is configured as V-tail as the jet engine exhaust is not affecting it. Its high Eigenmodes are well separated from wing flutter frequencies.

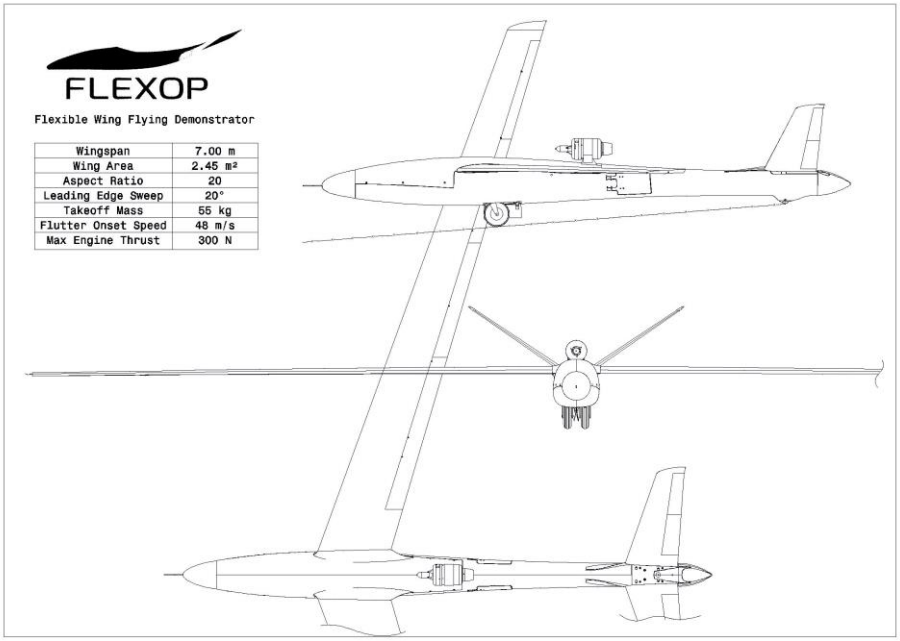

Figure 4: 3-side view of FLEXOP demonstrator aircraft after detailed design

Each wing half features four control surfaces of which the outermost one is used for flutter suppression. A custom made actuator moves the surface with sufficient bandwidth. The two innermost control surfaces serve as high lift devices during takeoff and landing. Attached to the flutter actuator is a rod where exchangeable masses for flutter tuning can be installed (Figure 5). A first flutter mode gets instable at 48.1 m/s and 7.95 Hz as a symmetric second bending form. The second mode follows at 50.5 m/s and 6.42 Hz as an antisymmetric first bending form. Divergence occurs at 62.5 m/s.

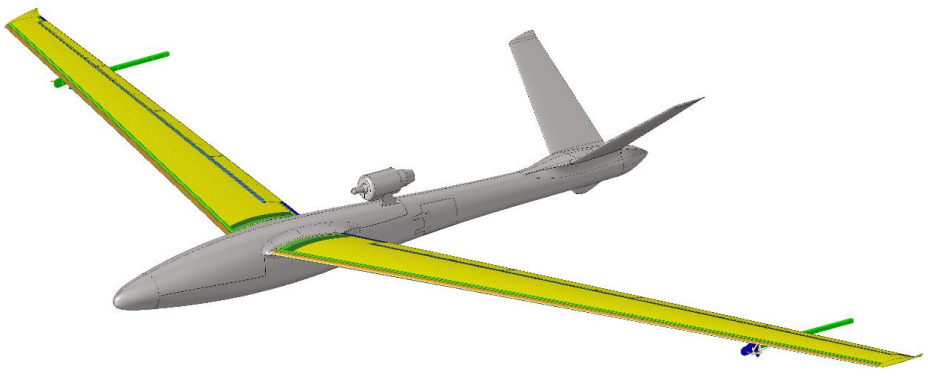

Figure 5: CAD Modell of FLEXOP demonstrator aircraft showing external flutter actuators with a rod for flutter trim mass installation possibilities

The elevator also consists of two surfaces. The splitting of the control surfaces is part of the redundancy concept. The aircraft's power supply, command and control architecture are designed to be robust against a single point of failure. In this failure case, controllability sufficient to perform an emergency landing is maintained. In a more severe failure scenario, like a structural failure due to flutter, a rescue parachute is opened. It leaves the aircraft through the detachable end cone. It also ensures that the aircraft stays within its permitted flight area in case of command link loss. The fuselage features a large canopy to enable convenient access to all systems needing ground service.

The final flutter wing structural design (Figure 6) is based on a twin spar solution, which are used as main load carrying structural components. Additional ribs are added to support the very flexible outer skin shell. Spars and ribs are designed as monolithic CFRP layup. The wing shell is predominantly used to adjust the torsional stiffness of the wing. Due to its lower material stiffness, GFRP is used. To afford enough local bending stiffness and prevent elasto-static instabilities, the skin is build up as foam core sandwich design. As mass saving aspects are considered, the sandwich design further supports a high lightweight potential solution.

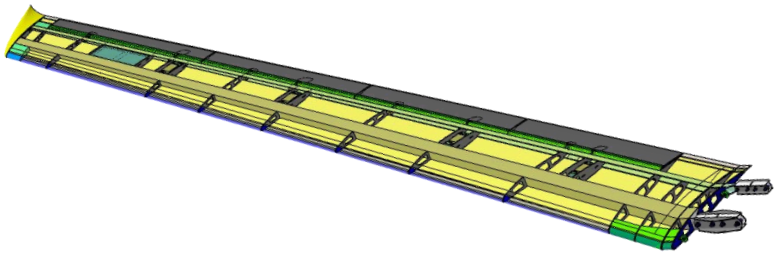

Figure 6: Structural design of the flutter wing (with invisible top skin)

B. Aeroelastically-Tailored Wing Design

Within the FLEXOP project two wing designs are derived to demonstrate the benefits of aeroelastic composite tailoring. The first design, referred to as the reference wing, serves as the baseline. It is derived using the more conventional balanced-symmetric laminates. In contrast to the reference wing, the second design, referred to as the tailored wing, is derived using unbalanced laminates, thus allowing a much larger design space and exploitation of composite coupling benefits. Both wings are optimized to obtain the best possible design given the applied constraints. This allows for a more conservative and realistic assessment of tailoring benefits.

1. Aeroelastic Tailoring Framework

The aeroelastic tailoring approach applied in this work is essentially a multi-fidelity procedure where the wing structure is optimized using an aeroelastic tailoring toolchain, developed at the Delft University of Technology (TUD) and DLR-Institute of Aeroelasticity (DLR). Such an approach is selected due to the very large number of optimization variables and constraints present in a typical optimization problem concerning aeroelastic tailoring. The following sequential approach is hence implemented and is summarized in Figure 7.

1. A low-fidelity beam-model based stiffness-optimization tool PROTEUS [13[15]. This step is used to perform initial design-studies and to explore the vast design-space. The optimized design from this step serves as the initial design for the second step in the toolchain.
2. A high-fidelity shell-model based genetic algorithm (GA) for stacking sequence optimization [16,17]. The outcome of this step is a refined wing design and the layup plan that is required for manufacturing.

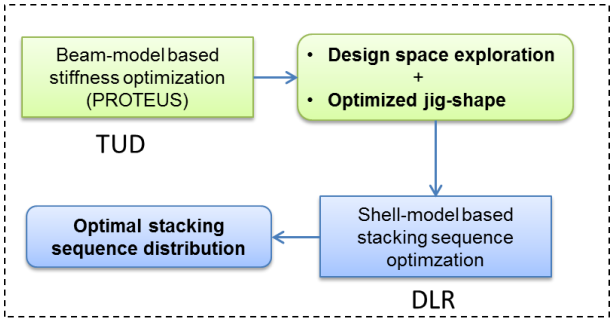

Figure 7: Two-step DLR-TUD aeroelastic tailoring framework

The idea underpinning such a two-step approach is that first, an extensive design-study is performed wherein effects of different material types, laminate reference coordinate system definitions and wingbox and rib layouts are quickly sifted through using the low-fidelity design tool. Additionally, the optimized design obtained from this step serves as the starting point in the second optimization step for faster overall convergence. The second optimization step depends on a shell-based NASTRAN FE model of a higher-fidelity which is incorporated in a discrete GA for stacking sequence optimization.

2. *Optimization Setup*

The objective of the design optimization is to minimize the structural mass of the conceived wings. To maintain a large enough design space while considering ease of manufacturability, the wing is split into 12×1 spanwise and chord-wise design regions as shown in Figure 8. The laminate stacking sequence in the upper and lower skin, and the front and the rear spar is optimized per design region while the laminates in the ribs are pre-defined. Additionally, the leading edge, trailing edge and flaps are not a part of the optimization exercise since they do not belong to the primary structure of the wing.

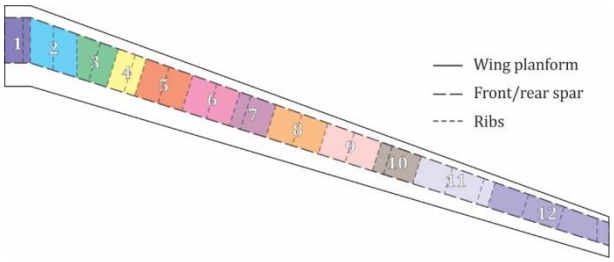

Figure 8 Distribution of wing design regions

To obtain a valid performance comparison between the reference and the tailored wing, a constraint on the 1g cruise shape is enforced in the optimization. This way it is ensured that the benefits due to aeroelastic tailoring do not compromise the aerodynamic performance of the designed wings. A linear twist distribution with 0° at the root and -2° at the tip, at 1g cruise is used as the 1g constraint. The optimization objectives, responses and load-cases are summarized in Table 1.

Table 1: Aeroelastic tailoring objectives and constraints

Optimization parameter	Value
objective	mass – minimization
outputs	blended stacking sequence jig-twist
physical constraints	laminate strength buckling tip-twist (at 1g cruise) static divergence aileron effectiveness, η > 15%
laminate constraints	10% rule [] symmetry ply contiguity (max. 4) $\pm$45° outer plies max. disorientation of 45° balance (for reference wing)
sizing load cases	+5g at 45m/S (TAS) -2g at 45m/s (TAS)

3. *Results*

The optimization results obtained from the first optimization step using PROTEUS, such as the optimal stiffness distribution and the jig shape twist pertinent to both the reference and the tailored wing have been already reported in [15]. The detailed results obtained from the high-fidelity step are presented in [18], hence only the main results and the comparison between the two result sets are presented here.

The final mass of the reference and the tailored wings is listed in Table 2. Two important points are evident. First, the tailored wing is almost 8% lighter than the reference in terms of structural mass. This weight saving is solely due to the relaxed laminate definition offered by the unbalanced laminates which allow for extension-shear and bend-twist couplings. The difference between the reference and the tailored wing in terms of stiffness distribution is illustrated in Figure 9 showing the polar distribution of the A_{11} term of the in-plane stiffness matrix in the upper skin. The highly anisotropic stiffness distribution in the tailored wing facilitates the bend-twist coupling that induces a wash-out effect upon increased aerodynamic loading as illustrated in Figure 10a. The wash-out redistributes the aerodynamic loads toward the inboard section of the wing depicted in Figure 10b. As a result, the root bending moments are alleviated. In a 5g and -2g maneuver the tailored wing experiences 6% and 11% lower root bending moments relative to the reference wing. The results for each load case are also summarized in Table 2. The reduced loads result in lesser thickness requirements as shown in Figure 11, leading to the savings in weight.

Second, it is seen that going from stiffness optimized design in the first design step to a stacking sequence design in the second design step some performance is lost both in terms of structural weight and load alleviation capabilities. The stiffness-optimal designs obtained in the first optimization step in both the reference and tailored wings are between 12-17% lighter than their stacking sequence counterparts. Also, the load alleviation capabilities of the tailored wing are reduced from 6% to 3% for the 5g load case and from 11% to 6% for the -2g load case. The observed performance loss is expected since the stacking sequence design is further constrained by the discrete steps of ply angles and thickness in addition to all the other optimization constraints applied already in the first design step. Additionally, the stacking sequence design includes the constraint of laminate blending and the additional guidelines important for the manufacturing of the laminates.

Table 2: Optimized mass and root-bending moment comparison for the reference and tailored wing design

	Mass (kg)	Root bending moment (Nm)		
		1g	5g	-2g
Stiffness-opt.† (reference)	5.884	304	1662	726
Stiffness-opt.† (tailored)	5.652 (0.96)	305 (1.00)	1555 (0.94)	647 (0.89)
Stacking seq.‡ (reference)	6.878	310.95	1697.65	-729.61
Stacking seq.‡ (tailored)	6.307 (0.92)	314.17 (1.01)	1651.86 (0.97)	-689.01 (0.94)

†PROTEUS optimization step
‡Stacking sequence optimization step

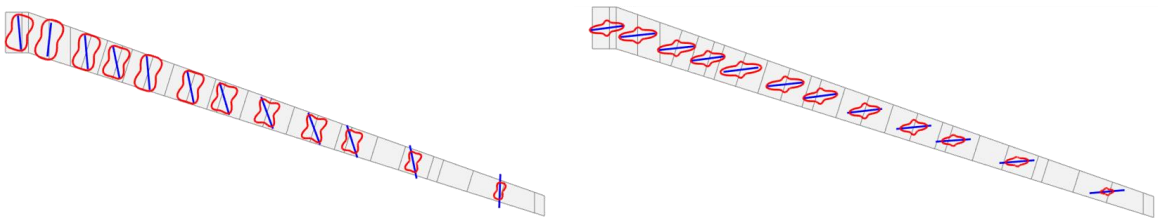

a) Reference wing b) Tailored wing

Figure 9: Polar distribution of the in-plane stiffness in the upper skin of the reference and tailored wing

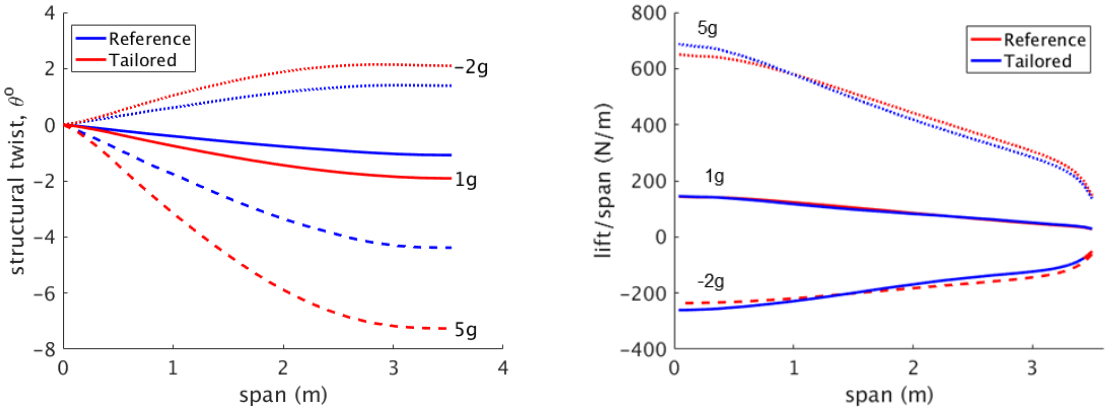

a) Torsional deformation b) Lift distribution

Figure 10: Spanwise torsional deformation and lift distribution for the reference and the tailored wing at selected maneuver loads

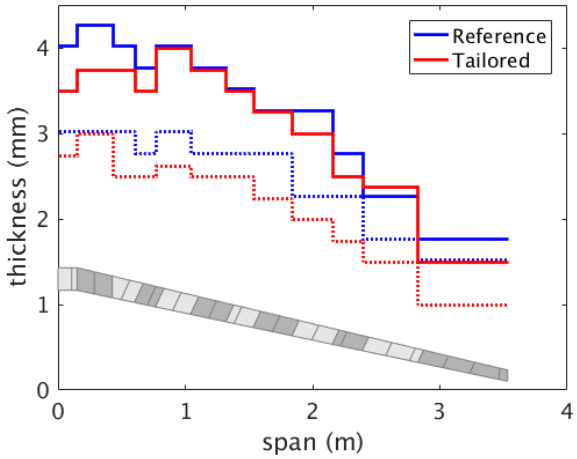

Figure 11: Spanwise laminate thickness distribution in the upper and bottom wing skin

III. FLEXOP UAV Testing

A. Ground Testing

In order to ensure the airworthiness of the assembled demonstrator, not only the structure has to be inspected and tested, but also the models developed by the project partners have to be validated before the first flight. Four test campaigns are planned for assessing the structural-dynamic models via static and vibrations tests. The assessment is split into the following parts: wing bending and torsion test for validation of the modelled structural stiffness; wing bending under limit load test for structural airworthiness; preliminary ground vibration testing using inertial measurement units integrated into the wings; ground vibration testing for dynamic structural model assessment and update. The tests have to be performed for every wing-set at least once.

1. Static tests

For the static tests involved in the model-updating process, prescribed loads are applied to both halves in a symmetric fashion. Discrete loads are applied by hanging weights at predetermined locations along the span of the wing. In order to appropriately account for the boundary conditions during the static tests, both left and right half of the wing are mounted in the test-stand as shown in Figure 12. The test-stand imitates the actual wing-fuselage connection as close as possible. Altogether 18 load-cases are tested for the different load-positions, load magnitudes and for bending- and torsion-dominant load cases. In addition, load clamps fitted at a given wing span-section are used to spread the load gradually into the wing structure to avoid causing any structural damage

due to local stress concentrations. The position of pre-defined markers on the wing is next recorded using a laser-tracking system. From the marker positions recorded without and with the loads, the displacements and twist at the marker points are calculated. The deformation results are then used in the model-updating processes.

For the static tests involved in the airworthiness tests, the wing is loaded with a 5g and -2g equivalent load by hanging sand bags at six span-wise locations on both wings (Figure 13). The equivalent loads are derived by introducing the deflected shape of the wing under the respective manoeuver loads through the loading at the discrete points. In such way the resulting shear force and the bending moment along the span are reconstructed. In the case of the -2g loads, the wing is flipped over before applying the loads.

Figure 12**: Attachment of reference wing to the test-stand (left), load-application for the static tests (right)**

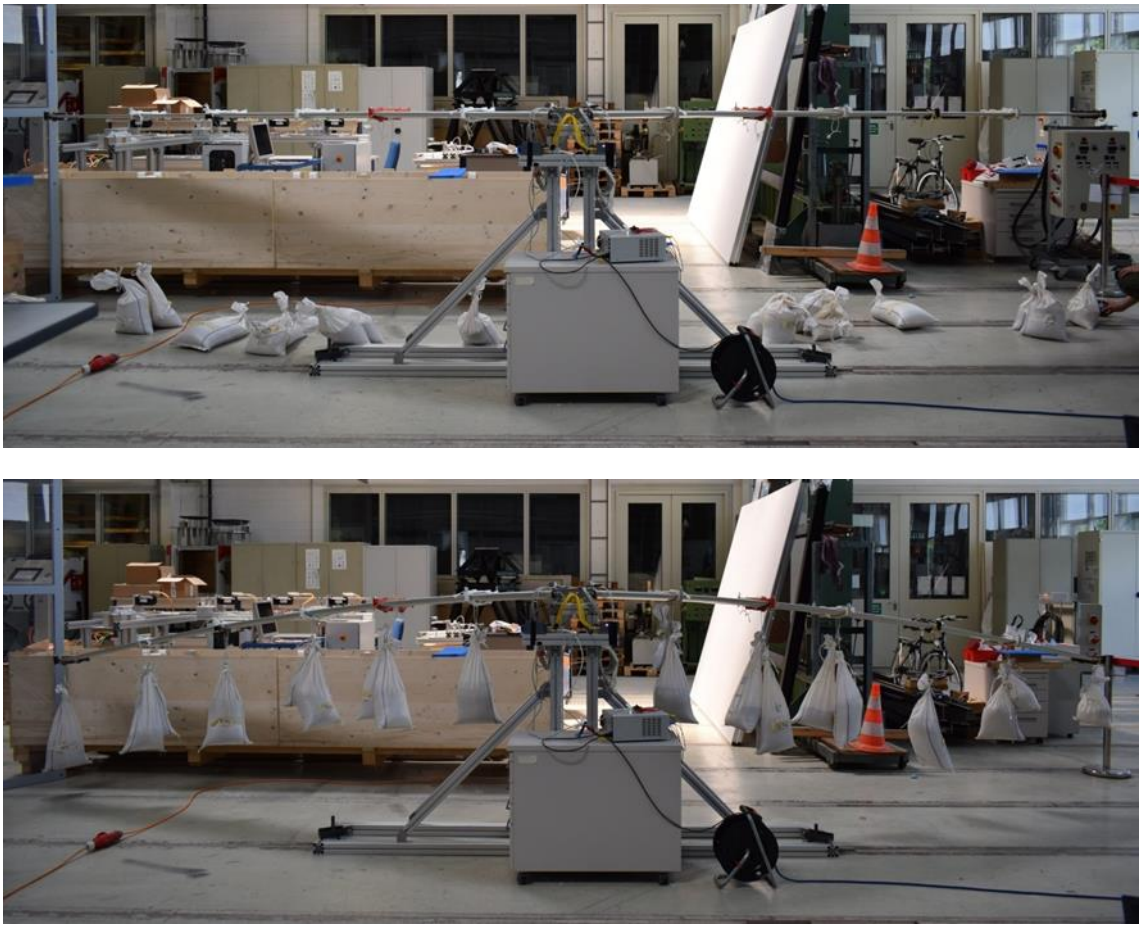

Figure 13: Airworthiness test of the reference wing - unloaded (above) and loaded (below)

2. Ground vibration tests (GVT)

The purpose of the preliminary GVT is to test the function of the integrated inertial measurement units (IMUs) and prepare a preliminary report for the full GVT performed later on. The instrumentation of a single wing already includes 12 integrated IMU sensors with a purpose of measuring real-time accelerations within the wing during flutter tests. Therefore it was initially decided to use these sensors as means of preparation for the full GVT. These tests were performed with a completely assembled demonstrator on a rigid test stand with functioning logging and actuator systems. The excitation is done with a calibrated constant-force hammer to also provide an input signal. For the full GVT the FLEXOP demonstrator will be instrumented with accelerometers over the wings, fuselage and empennage. The aircraft will then be suspended on elastic strings and excited with an impulse hammer. From the time-response of the accelerometers, a modal analysis will be performed to obtain the eigen frequencies, mode shapes and damping corresponding to each of the modes. The results will then be used to update the dynamic models used during the design processes. Both ground vibration tests will be performed for all three wing configurations.

B. Flight Testing

As all flights have to be performed under visual line of sight, a racetrack pattern has been chosen for flutter testing (Figure 14, left) [9]. The pattern splits up into turn, acceleration, test leg, deceleration, turn and cruise back. The test leg used for flutter testing is only flown once per circuit to profit from an eventual headwind component. The speed is reduced in the turn to avoid flutter onset due to increased load factor and in order to enable turns at reasonable bank angle and radius. During the test leg the structure is excited. The primary excitation method will be an impulse on the wing's outermost control surfaces. In a secondary scenario, a control surface impulse is not sufficient to activate all relevant modes and thus a frequency sweep signal is used [10]. The excitation sweep is performed on a wing control surface not used for active flutter control. The response of the aircraft is measured by acceleration and gyroscopic sensors and the damping factor can be calculated. The first test will be at a speed well below the flutter border. All subsequent higher airspeeds are determined by the damping and damping trend of the previous tests. Therefore sensor data will be transmitted to the ground and analyzed live. As a safety measure a real time flutter indicator can trigger a deceleration of the aircraft if a damping limit or oscillation threshold is exceeded. To increase the available test leg time, the engine will be kept at high throttle setting during the pre-test turn and the speed will be controlled via the airbrakes. In such way the slow dynamic response of the engine can be eliminated. Due to the complex mission profile for flutter testing, autopilot will be used for flying the test segments. However, the pilot will always be able to take the command from the autopilot.

For the load alleviation test circles with defined speed and bank angle are flown (Figure 14, right).

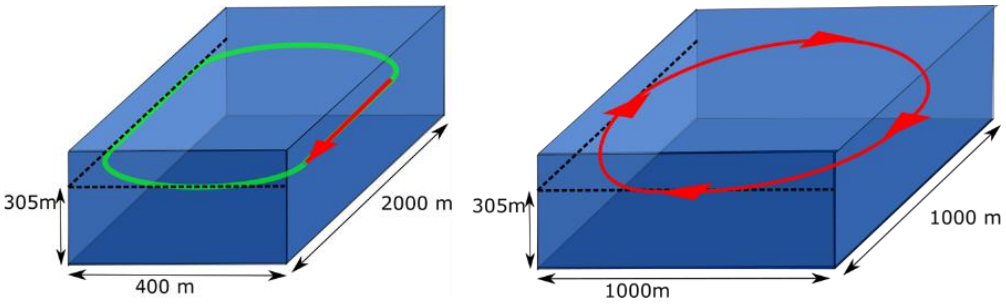

Figure 14: Racetrack for flutter testing (left) and circle mission for load alleviation tests (right)

As a preparation for the flight tests, a flight simulator is used. The simulator presents the flown aircraft on the screen in exactly the same way it would be seen by the pilot (Figure 15). The simulation environment corresponds to the actual airport that will host the test flights and the pilot uses the same transmitter for the command inputs. The flight test crew has access to almost identical telemetry software as would be used during the flight tests. This helps to define the various procedures for communication, mission and emergency scenarios saving time required at the airport.

Figure 15. Flight test simulation for operational training.

There are three telemetry links designed for the aircraft each having a different purpose- operations telemetry link, safety and engineering data telemetry link and pilot information link. MissionPlanner [19] software is used for the operations link, displaying all the information regarding the position and attitude of the aircraft as well as the flight box limits. The safety and engineering data telemetry link monitors position and temperature of every actuator on the aircraft, the engine data, fuel status and accelerometer values. The status of the flight control computer hardware parts is displayed here via status indicators. These two telemetry links are monitored inside the ground control station by two flight test engineers. The third telemetry link is transmitted directly from the aircraft to the pilot, who is positioned at the runway, and informs him about the airspeed and altitude of the aircraft.

C. In Flight Wing Shape Measuring

In order to assess the developed load alleviation and flutter suppression mechanisms, the following methods for the calculation of the wing shape and structural loads were developed. This is achieved by measuring strain on various locations on the wings, using multiple arrays of optical strain sensors in the form of Fiber Bragg Gratings (FBGs) and processing the data accordingly.

Two numerical, geometry-based methods were developed for the calculation of the wing shape along the wing's axis, particularly vertical displacement (y), bending slope (θ) and torsion twist (φ). The first uses a series of rosettes on the upper and lower wing skins, along its axis. The second uses a small number of FBGs located on the front and rear spars and oriented along each spar's axis.

A data-based method was developed for the calculation of structural loads along the wing's axis, particularly shear force (V), bending moment (M) and torsion (T). The method involves the calculation of the wing's equivalent stiffness matrix and its use, along with raw strain measurements, to calculate structural loads. A numerical platform was also developed, based on the finite element (FE) model of the flexible wing, to assess the method's robustness and applicability, serving a as a virtual testing environment.

The ability to capture the operations as matrices, as well as their inherent robustness in the presence of realistic, imperfect measurements, are the two key advantages of the developed methods. The former allows a better understanding of the model as a mathematical structure, as well as advanced embedding capabilities. The latter is a promising indication that these methods can be applied effectively on the physical structure, using experimental data, which is what future research will mainly focus on.

1. Strain Sensor Layout Design and Integration

Three sensor layouts were prepared, one for each pair of wings. The three layouts consist of three basic sensor configurations. Additionally temperature sensors were included to account for thermal strains during flight. The layouts were updated between pairs of wings based on the experience acquired during the process.

The first configuration is the "classic strain rosette", consisting of three FBGs, each measuring normal strain at 0º, 45º and 90º, with respect to the wing's axis. Rosettes were placed on both upper and lower skins, along the wing's axis. The second configuration is the "spar FBG", measuring normal strain along the spar's axis. Spar FBGs were placed on both upper and lower skins. The third configuration is the "reduced strain rosette", consisting of two FBGs instead of three, omitting the sensor measuring lateral strain. This adaptation was made in an attempt

to reduce the number of strain sensors and hence the cost, whilst maintaining accuracy in the calculations. Given the geometry and loading of the system, the particular sensor orientation added little to the performance of the rosette and was deemed negligible. The three sensor configurations are presented in Figure 16, FBGs shown in red.

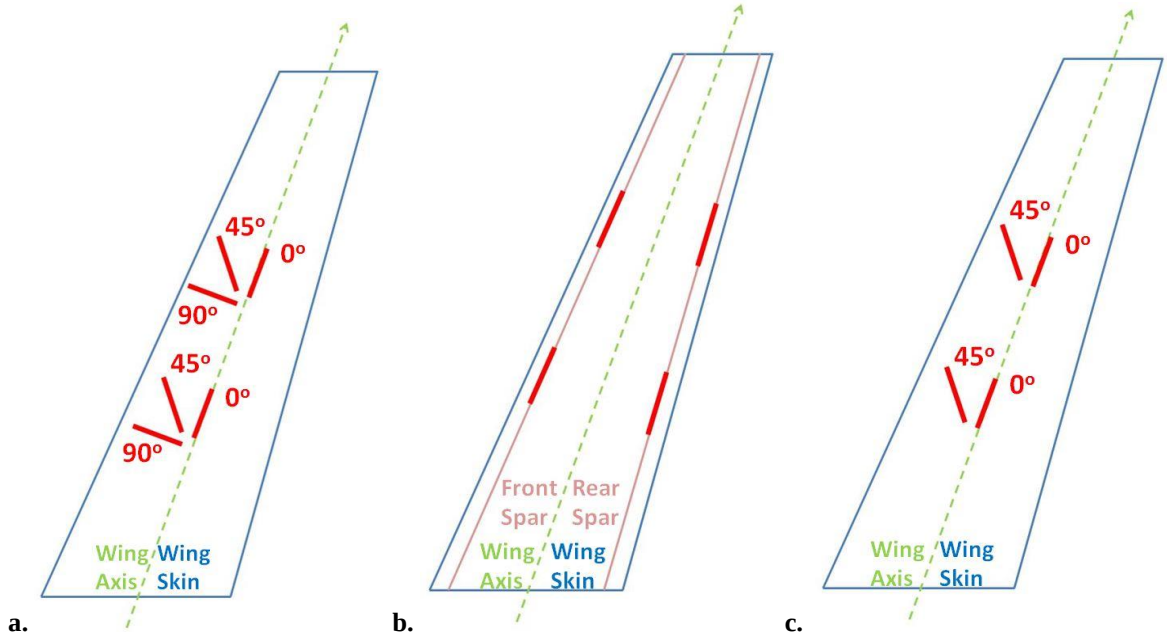

a. **b.** **c.**

Figure 16: a. Classic strain rosette b. Spar FBG c. Reduced strain rosette

Each wing pair uses a combination of the three strain configurations. The baseline wing is equipped with 20 classical strain rosettes per wing skin. The tailored wing has an additional 8 spar FBGs along each spar, for a total of 16 per skin. In the flutter wing the classical rosettes were replaced by 10 reduced strain rosettes. Finally, 10 and 9 temperature sensors were included in all skins of the first two and the third wing pair respectively. The three sensor layouts are summarized in Table 3.

Table 3: Summary of sensor layouts

	Classic Strain Rosettes		Spar FBGs		Reduced Strain Rosettes		Temperature Sensors	
Wing type	Upper Skin	Lower Skin	Upper Skin	Lower Skin	Upper Skin	Lower Skin	Upper Skin	Lower Skin
baseline	20	20					10	10
tailored	20	20	16	16			10	10
flutter			16	16	10	10	9	9

2. Wing Shape Calculation

Two methods were developed for the calculation of the wing shape along the wing's axis. Each method utilizes a different set of sensors and calculates the wing shape independently. The two methods are finally assessed against each other.

The first method uses strain measured by the rosettes located on the wing's axis. Axial strain (ε) is used to calculate y and θ and shear strain is used to calculate φ. Two simple mathematical models are constructed, relating strain to displacement, using geometrical factors and integration. The models can be expressed in matrix form, capturing the property of numerical integration, using the trapezoid rule, as a summation operator, as seen in eq. (1) and (2).

$$I = \int_a^b f(x)dx = \sum_{i=1}^{N-1} \frac{1}{2}\left(f_i(x) + f_{i+1}(x)\right)\Delta x_i = \frac{1}{2}\Delta x_1 f_1(x) + \frac{1}{2}(\Delta x_1 + \Delta x_2) f_2(x) + \cdots + \frac{1}{2}\Delta x_{N-1} f_N(x) \quad (1)$$

$$I = \left[\frac{1}{2}\Delta x_1 + \frac{1}{2}(\Delta x_1 + \Delta x_2) + \cdots + \frac{1}{2}\Delta x_{N-1}\right] \cdot [f_1(x)\, f_2(x) \cdots f_N(x)]^T = \vec{k} \cdot \vec{f}^{\,T} \tag{2}$$

The first model is based on the Classical Beam Theory, given by eq. (3), relating normal stress (σ) to the beam's curvature (1/R), Young's Modulus (E) and section height (h). This expression is manipulated to yield expressions for θ and y as functions of normal strain and a geometrical factor, as seen in eq. (4) and (5).

$$\frac{\sigma}{h} = \frac{E}{R}, \sigma = E\varepsilon \rightarrow \frac{1}{R} = \frac{\varepsilon}{h} \tag{3}$$

$$\theta(x) = -\int_0^x \frac{1}{R(x)}dx = -\int_0^x \frac{\varepsilon(x)}{h(x)}dx = M_\theta^1 \cdot \vec{\varepsilon} \tag{4}$$

$$y(x) = -\iint_0^x \frac{1}{R(x)}dx = -\iint_0^x \frac{\varepsilon(x)}{h(x)}dx = M_y^1 \cdot \vec{\varepsilon} \tag{5}$$

The matrices M_y^1 and M_θ^1 are linear operators capturing the geometry of the physical system, as well as double and single integration as a summation. This is outlined in eq. (6), indicating the structure of the matrix. The key factor is the approximation of the wing as a cantilever beam, the indexing of the nodes increasing towards the wing tip.

$$\vec{y} = M_y^1 \cdot \vec{\varepsilon} \rightarrow \begin{bmatrix} y_1 \\ y_2 \\ y_3 \\ \vdots \\ y_{N-1} \\ y_N \end{bmatrix} = \begin{bmatrix} m_{y,11}^1 & 0 & 0 & \cdots & 0 & 0 \\ m_{y,11}^1 & m_{y,11}^1 & 0 & \cdots & 0 & 0 \\ m_{y,11}^1 & m_{y,11}^1 & m_{y,11}^1 & \cdots & 0 & 0 \\ \vdots & \vdots & \vdots & \ddots & \vdots & \vdots \\ m_{y,11}^1 & m_{y,11}^1 & m_{y,11}^1 & \cdots & m_{y,11}^1 & 0 \\ m_{y,11}^1 & m_{y,11}^1 & m_{y,11}^1 & \cdots & m_{y,11}^1 & m_{y,11}^1 \end{bmatrix} \begin{bmatrix} \varepsilon_1 \\ \varepsilon_2 \\ \varepsilon_3 \\ \vdots \\ \varepsilon_{N-1} \\ \varepsilon_N \end{bmatrix} \tag{6}$$

The second model is based on similar models relating shear strain (γ) to the rate of change of twist along the wing's axis (dφ/dx), using a geometrical factor (c), as seen in eq. (7). Such models exist for elliptic and rectangular beam sections, the two shapes mostly resembling a wing section. Similar to the previous model, a matrix M_φ^1 is defined, capturing the linear operation relating γ to dφ/dx, shown in eq. (8). The factor c is calculated numerically using the FE model, in the absence of reliable analytical models.

$$\gamma = c \cdot \frac{d\varphi}{dx} \rightarrow \frac{d\varphi}{dx} = \frac{\gamma}{c} \tag{7}$$

$$\varphi(x) = \int_0^x \frac{\gamma(x)}{c(x)}dx = M_\varphi^1 \cdot \vec{\gamma} \tag{8}$$

The second method uses strain measured by the spar FBGs along the spars' axes. Normal strain is used to measure y_f and y_r as well as θ_f and θ_r on the front and rear spar respectively. Assuming the section of the wing remains undeformed, a geometrical model was developed, relating the deformation of the two spars to the deformation of the wing's axis. This method is expected to yield a more accurate estimate of twist, since the previous method relied on shear strain which is expected to be minimal, given the anticipated dominance of bending over torsion

In the absence of experimental data, all the previously mentioned matrices are calculated using the developed FE model, relating virtual strain data to virtual displacement data. The performance of the two methods can be assessed in Figure 17, by comparing the shape (y, θ and φ) calculated by each method relative to the shape calculated directly by the FE model.

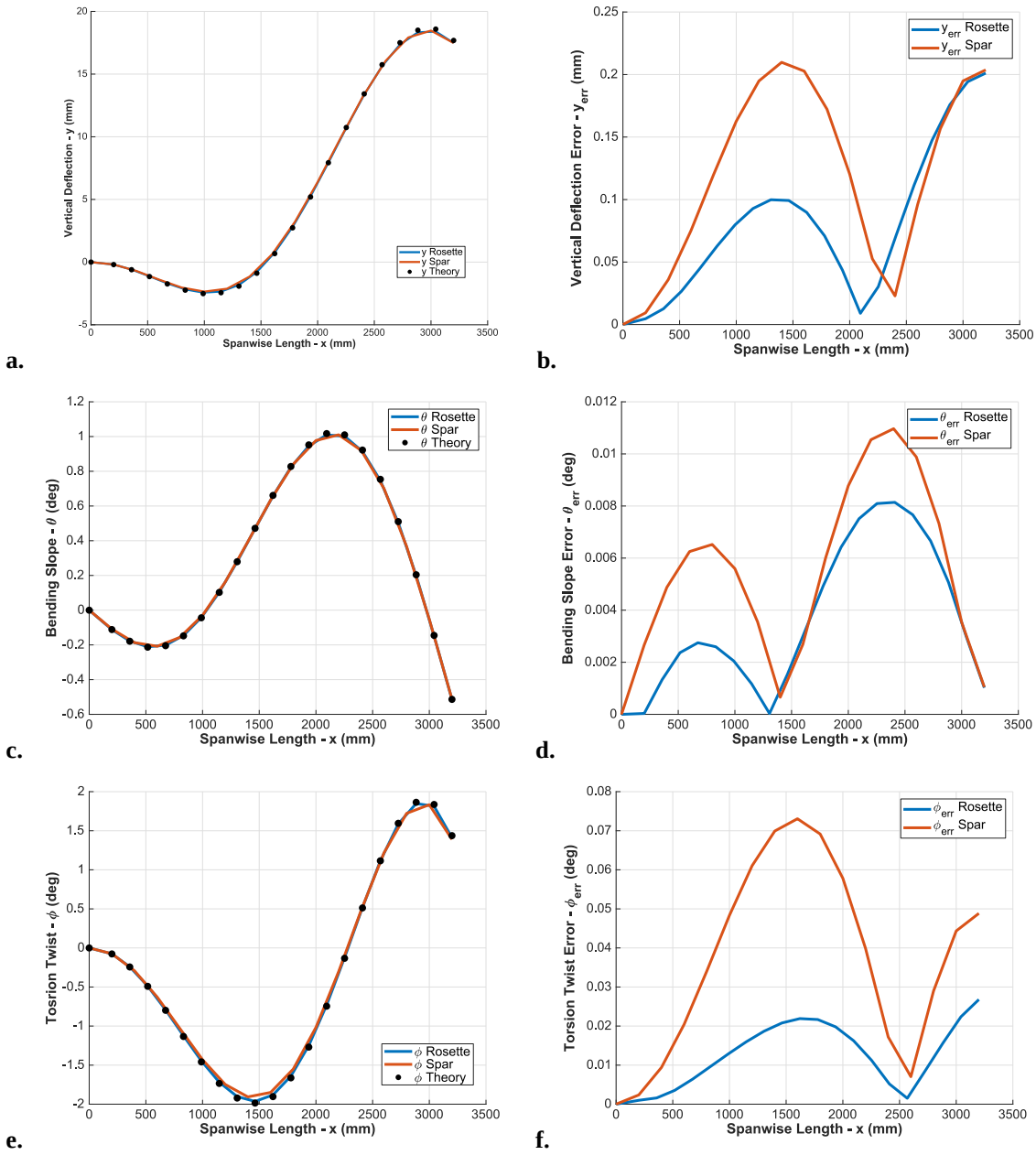

Figure 17: Axial Variation of a. Vertical Deflection b. Vertical Deflection Error c. Bending Slope d. Bending Slope Error e. Torsion Twist f. Torsion Twist Error

By observing the graphs on Figure 17, it is evident that both methods are able to capture the wing shape accurately; y is calculated within 0.2 mm, θ within 0.01° and φ within 0.07°. As expected, the first model is 2-3 times more accurate than the second, which involves more calculations, introducing additional error. In addition, more strain measurements were used in the first model, a key parameter in methods involving numerical integration. Nevertheless, the second method is expected to be more robust in practice, using normal strain rather than shear strain.

The methods remain to be validated experimentally using the static test data and applied on the flight test data for the calculation of wing shape during flight.

3. Structural Load Calculation

A method was developed for the calculation of structural loads along the wing's axis, using the FBG strain measurements. The equivalent stiffness matrix (K) is first calculated using calibration strain data from specifically selected load cases, during the static tests. The matrix is then used in conjunction with raw strain data to calculate the shear force, bending moment and torsion moment along the wing's axis.

The developed method is based on the work of Skopinski et al. [21] where a generalized framework was established for the calibration of strain-gage installations and the accurate calculation of flight loads. The greatest advantage of the referenced method is the ability to work with raw strain data, hence incorporating the anticipated imperfections of the sensors in the calibration, avoiding simplifications which would deviate from the real physical system. Furthermore, a recent study by Viana [22] confirmed the suitability of FBGs as strain-gages in such a framework, by capturing structural loads reliably.

Some key adaptations were made, to address the present physical system. First of all, it is assumed that local bending moment and torsion are linearly related to the strain tensor at this location, as seen in eq. (9). Therefore, a set of secondary stiffness matrices (Q^i) is defined, one for each strain station (i) along the wing's axis. It must be noted that normal strain at 45° is used (as measured by the corresponding FBG), rather than shear strain. The secondary matrices Q^i combine to form the principal matrix K, as seen in eq. (10).

$$\overrightarrow{f^i} = Q^i \cdot \overrightarrow{\varepsilon^i} \rightarrow \begin{bmatrix} M^i \\ T^i \end{bmatrix} = \begin{bmatrix} q_{11}^i & q_{12}^i & q_{13}^i \\ q_{21}^i & q_{22}^i & q_{23}^i \end{bmatrix} \begin{bmatrix} \varepsilon_0^i \\ \varepsilon_{90}^i \\ \varepsilon_{45}^i \end{bmatrix} \tag{9}$$

$$\vec{f} = K \cdot \vec{\varepsilon} \rightarrow \begin{bmatrix} \overrightarrow{f^1} \\ \overrightarrow{f^2} \\ \vdots \\ \overrightarrow{f^N} \end{bmatrix} = \begin{bmatrix} Q^1 & 0 & \cdots & 0 \\ 0 & Q^2 & \cdots & 0 \\ \vdots & \vdots & \ddots & \vdots \\ 0 & 0 & \cdots & Q^N \end{bmatrix} \begin{bmatrix} \overrightarrow{\varepsilon^1} \\ \overrightarrow{\varepsilon^2} \\ \vdots \\ \overrightarrow{\varepsilon^N} \end{bmatrix} \tag{10}$$

Furthermore, shear force is calculated as the derivative of bending moment with respect to axial position, as seen in eq. (11). The relation between V and M can also be captured by a matrix, D. All the above adaptations are in accordance with Classical Beam Theory.

$$V = -\frac{dM}{dx} \qquad \vec{V} = D \cdot \vec{M} \tag{11}$$

The calculation of the Q^i matrices involves the use of a number of load cases of known local load and strain distributions. The wing is loaded with weights (W) at known positions, which are treated as point loads. Hence, given their axial distance (Δy) from the sensors and their lateral distance (Δx) from the wing's axis, the values of M^i and T^i are calculated, as shown in eq. (12).

$$M^i = W\Delta y^i \qquad T^i = W\Delta x^i \tag{12}$$

Treated as a cantilever beam, sensors are loaded and measure strain from loads applied at a further axial position. Loads applied closer to the wing root do not affect the particular sensor. Moreover, in the case of multiple applied loads, the total M and T is calculated. For each sensor, the structural loads and measured strains at each load case (j) are expressed in matrix form (S_f and S_ε) as seen in eq. (13). Finally, a least squares approximation is performed, using the pseudo-inverse of the matrix of S_ε, and the corresponding Q^i is calculated.

$$\begin{aligned} S_f^i = Q^i S_\varepsilon^i \rightarrow & \begin{bmatrix} M_1^i & M_2^i & \cdots & M_j^i & \cdots & M_N^i \\ T_1^i & T_2^i & \cdots & T_j^i & \cdots & T_N^i \end{bmatrix} \\ = & \begin{bmatrix} q_{11}^i & q_{12}^i & q_{13}^i \\ q_{21}^i & q_{22}^i & q_{23}^i \end{bmatrix} \begin{bmatrix} \varepsilon_{0,1}^i & \varepsilon_{0,2}^i & \cdots & \varepsilon_{0,j}^i & \cdots & \varepsilon_{0,N}^i \\ \varepsilon_{90,1}^i & \varepsilon_{90,2}^i & \cdots & \varepsilon_{90,j}^i & \cdots & \varepsilon_{90,N}^i \\ \varepsilon_{45,1}^i & \varepsilon_{45,2}^i & \cdots & \varepsilon_{45,j}^i & \cdots & \varepsilon_{45,N}^i \end{bmatrix} \end{aligned} \tag{13}$$

The robustness and applicability of this method was assessed using a numerical platform developed to serve as a virtual testing environment. An equivalent compliance matrix was extracted via the method of static condensation [20], capturing the FE model's behavior as a linear elastic structure with great accuracy, relating applied loads at 63 locations on the wing to strains on the positions of the 20 rosettes of the baseline wing. This enabled the easy generation of virtual load cases and strain data.

The virtual data was adapted to approximate realistic imperfections in the experimental data; such a case study is presented below. Realistic measurement noise of the order of 3% was added to the strain data, as expected from the FBGs. In addition, the method was performed whilst omitting measurements of strain, hence emulating the presence of faulty FBGs; approximately 30% of FBGs were randomly selected and omitted from all over the wing. The effect of combining two rosettes from both skins into one strain sensor was also examined. The expression relating structural loads to strain, was therefore adapted to account for these changes, as seen in eq. (14). In this case, the upper and lower skin rosettes are missing the 45° and 90° FBGs respectively.

$$\begin{bmatrix} M^i \\ T^i \end{bmatrix} = \begin{bmatrix} q_{11}^i & q_{12}^i & q_{14}^i & q_{16}^i \\ q_{21}^i & q_{22}^i & q_{24}^i & q_{26}^i \end{bmatrix} \begin{bmatrix} \varepsilon_{u,0}^i \\ \varepsilon_{u,90}^i \\ \varepsilon_{l,0}^i \\ \varepsilon_{l,45}^i \end{bmatrix} \tag{14}$$

Finally, the number of load cases required for the calculation of K was limited to 8, which would correspond to a manageable static test. The load cases were designed so as to emulate dominant bending or dominant torsion. The performance of individual skins (upper, lower) as well as the combination of the two is presented in Figure 18, for a combined case of bending and torsion.

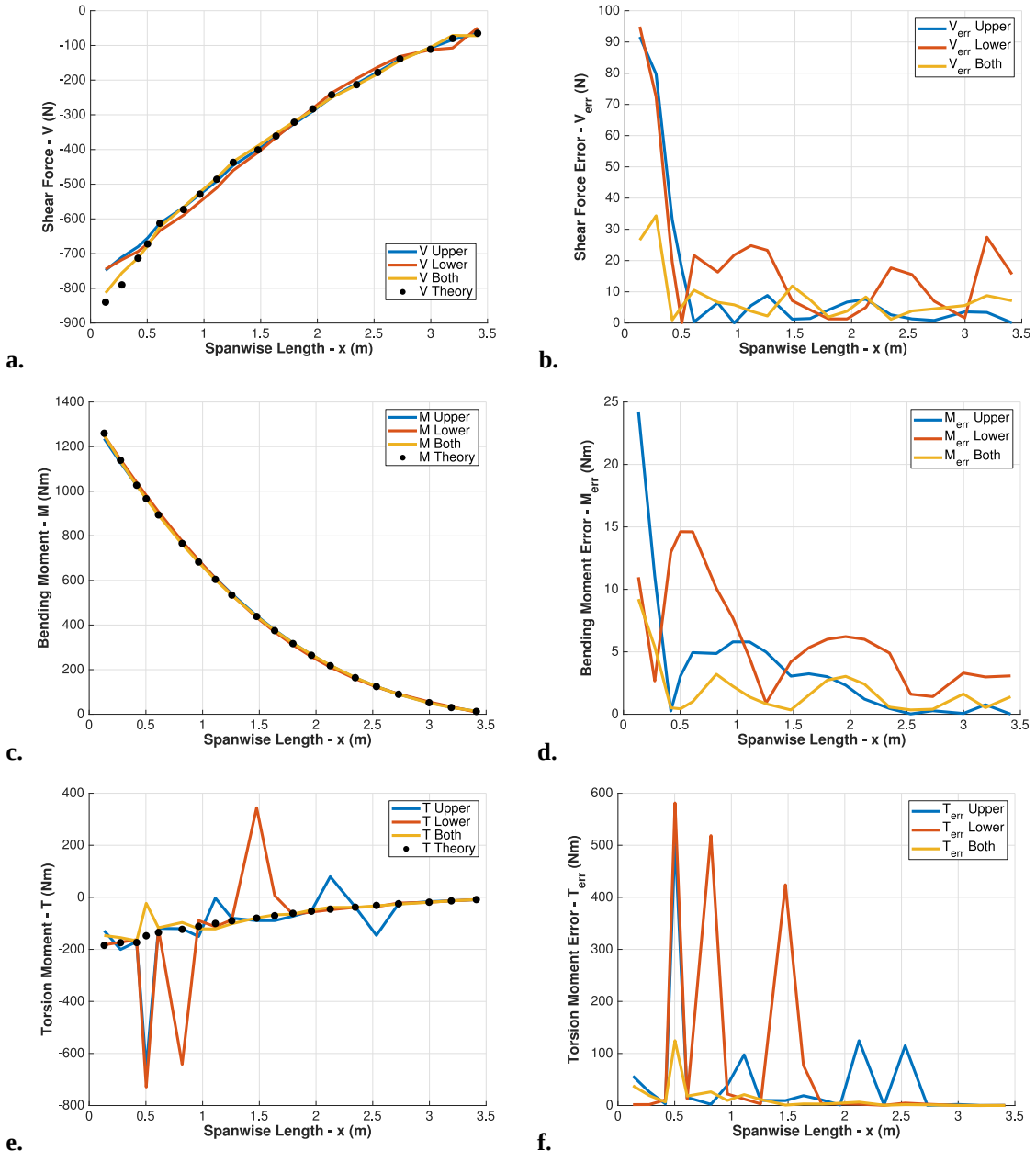

Figure 18: Axial Variation of a. Shear Force b. Shear Force Error c. Bending Moment d. Bending Moment Error e. Torsion Moment f. Torsion Moment Error

All three load distributions are calculated within an error of 20 N or Nm. This is the result of measurement noise which manifests as an absolute error. As a result, loads are calculated more precisely near the wing root (less than 5% error) rather than the tip (up to 10% error), being greater in magnitude. Similarly, dominant loads of greater magnitude are calculated more reliably than less significant loads; in the above case, estimates of M and V, of

order ~1000, are more precise than estimates of T, of order ~200. Alternatively, the method would calculate T more accurately for a load case of dominant torsion over bending.

The robustness of the method in the presence of faulty sensors must also be noted. Faulty FBGs oriented at 0° and 90° to the wing's axis have no observable effect in the calculation of K and the loads. However, FBGs oriented at 45° maintain a key role in the calculation of T, as can be seen in Figure 18e, 4f; whilst T is calculated reliably in general, it fails completely in the absence of these sensors. Nevertheless, if a functional 45° FBG is present in either skin, the combination of upper and lower rosettes is able to calculate T. The sole poor estimate of T is found at length ~0.5 m, where both 45° FBGs were faulty.

Additionally, a key factor in obtaining an accurate estimate of V was the use of a smoothing operator on the distribution of M. Though this does not reduce the error in that distribution, it helps capture its shape more accurately, which is vital in the calculation of the derivative, as seen in eq. (11).

The methods remain to be validated experimentally using the static test data and applied on the flight test data for the calculation of structural loads during flight.

IV. Conclusion

An Aircraft design process to design a demonstrator with flexible wing technology has been set up and applied by TUM. The design-driving aeroelastic behavior has been considered with high fidelity already at early design stages. Precise methods are required to model an aircraft's aeroelastic characteristics which need to be arranged in the right order for the aircraft design process. The validation of the methods is ongoing with the help of static and ground vibration tests and later on flight testing.

With the experiences made so far the following improvements are suggested:

- Currently the arrangement of tools lacks automation. The manually performed iterations between tool blocks do not allow a high number of iterations. As a consequence convergence errors are rather high.
- Static aeroelastic deformation is highly relevant during aircraft design. Stall speed, speed limit, aerodynamic performance, handling characteristics, aircraft trimability and the necessity of flaps is dependent on it. Hence, aeroelastic trim calculations have to be part of the conceptual design phase already. In the presented design process, aircraft performance and stall prediction is only available for a rigid wing aircraft with design wing shape.

A joint DLR – TUD aeroelastic tailoring framework is applied to derive an optimum design for the reference and the tailored wing. In order to enable a fair demonstration of aeroelastic tailoring, the reference wing is designed using conventional balanced-symmetric laminates, while the tailored wing is designed using unbalanced laminates, thus allowing for better use of the beneficial bending-torsion coupling available in composite laminates. The wing-box comprising of upper and lower skins, front and rear spars, is optimized and the optimization results show a weight saving potential of ~8% when comparing the tailored with the reference design.

The methodology and planning for testing the structure and systems of the assembled demonstrator have been developed. During the tests, the measurement systems are being tested and calibrated in order to get them ready for the first flight. At the time of writing, the airworthiness test of the baseline wing showed that the wing can sustain the limit loads without any detectable structural damage and is therefore safe to operate. The installed IMU sensors perform as required. The fibre-bragg-based wing deformation measurement system works with minor deficiencies. The flight simulator was discussed to be of great value while preparing for operations within the airport. Currently the ground testing is ongoing. The maiden flight with the baseline wing is expected to commence this spring.

Acknowledgments

This project has received funding from the European Union's Horizon 2020 research and innovation program under grant agreement n◦ 636307.

References

[1] FLEXOP Consortium, "Horizon 2020: Proposal SEP 210181869 - FLEXOP," 2014.

[2] "FLEXOP Project Homepage," https://flexop.eu/news.

[3] Meddaikar, Y., Dillinger, J., Klimmek, T., Krüger, W., Wüstenhagen, M., Kier, T., Hermanutz, A., Hornung, M., Rozov, V., Alderman, J., Takarics, B., Vanek, B., "Aircraft Aeroelastic Modelling of the FLEXOP Unmanned Flying Demonstrator," AIAA Atmospheric Flight Mechanics Conference, AIAA SciTech Forum. San Diego, California. Jan.2019. (Submitted).

[4] Luspay, T., Ossmann, D., Baar, T., Teubl, D., Vanek, B., Pusch, M., Wuestenhagen, M., Kier, T., Waitman, S., Ianelli, A., Andres, M., Lowenberg, M., "Flight control design for a highly flexible flutter demonstrator," AIAA Atmospheric Flight Mechanics Conference, AIAA SciTech Forum. San Diego, California. Jan. 2019. (Submitted).

[5] Kotikalpudi, A., Danowsky, B. P., Schmidt, D. K., Gupta, A., and Regan, C., "Real-Time Shape Estimation for a Small Flexible Flying-Wing Aircraft," AIAA Atmospheric Flight Mechanics Conference, AIAA SciTech Forum. San Diego, California. Jan. 2019. (Submitted).

[6] Zhao, W., Gupta, A., Miglani, J., Regan, C. D., Kapania, R. K., and Seiler, P. J., "Finite Element Model Updating of Composite Flying-wing Aircraft using Global/Local Optimization," AIAA Atmospheric Flight Mechanics Conference, AIAA SciTech Forum. San Diego, California. Jan. 2019. (Submitted).

[7] Schmidt, D. K., Danowsky, B. P., Kotikalpudi, A., Seiler, P. J., and Kapania, R. K., "Flight-Dynamics, Flutter Analysis, and Control of MDAO-Designed Flying-Wing Research Drones," AIAA Atmospheric Flight Mechanics Conference, AIAA SciTech Forum. San Diego, California. Jan. 2019. (Submitted).

[8] Bundesministerium der Justiz und Verbraucherschutz, "Luftverkehrsordnung (LUftVO) §19 Verbotene Nutzung des Luftraums," 29 December 2015. [Online]. Available: https://www.gesetze-im-internet.de/luftvo_2015/__19.html.

[9] Stahl, P., Sendner, F.-M., Hermanutz, A., Rößler, C., and Hornung, M., "Mission and Aircraft Design of FLEXOP Unmanned Flying Demonstrator to Test Flutter Suppression within Visual Line of Sight," 17th AIAA Aviation Technology, Integration, and Operations Conference, American Institute of Aeronautics and Astronautics, Reston, Virginia, 2017.

[10] P. Farell and T. Ryall, "Flight Flutter Test Techniques at ARL - Aircraft Structures Technical Memorandum 569," Commonwealth of Australia, Melbourne, 1990

[11] Rößler, C., Conceptual Design of Unmanned Aircraft with Fuel Cell Propulsion System, München: Verlag Dr. Hut, 2012

[12] Sendner, F., Rößler, C., Hornung, M., "Designing an UAV Propulsion System for Dedicated Acceleration and Deceleration Requirements,"17th AIAA Aviation Technology, Integration, and Operations Conference, 07.06.17, Denver, Colorado, USA"

[13] N. P. M. Werter and R. De Breuker, "A novel dynamic aeroelastic framework for aeroelastic tailoring and structural optimisation," Compos. Struct., vol. 158, pp. 369–386, Dec. 2016.

[14] R. De Breuker, M. M. Abdalla, and Z. Gurdal, "A Generic Morphing Wing Analysis and Design Framework," J. Intell. Mater. Syst. Struct., vol. 22, no. 10, pp. 1025–1039, 2011.

[15] J. Sodja, N. Werter, and R. De Breuker, "Design of a flying demonstrator wing for manoeuvre load alleviation with cruise shape constraint," in 2018 AIAA/ASCE/AHS/ASC Structures, Structural Dynamics, and Materials Conference, 2018, no. 210049.

[16] J. K. S. Dillinger, T. Klimmek, M. M. Abdalla, and Z. Gürdal, "Stiffness Optimization of Composite Wings with Aeroelastic Constraints," J. Aircr., vol. 50, no. 4, pp. 1159–1168, 2013.

[17] Y. M. Meddaikar, F. X. Irisarri, and M. M. Abdalla, "Laminate optimization of blended composite structures using a modified Shepard's method and stacking sequence tables," Struct. Multidiscip. Optim., vol. 55, no. 2, pp. 535–546, 2017.

[18] M. Y. Meddaikar, J. K. S. Dillinger, J. Sodja, and R. De Breuker, "FLEXOP – APPLICATION OF AEROELASTIC TAILORING TO A FLYING DEMONSTRATOR WING," in DLRK 2018, 2018, pp. 1–10.

[19] ArduPilot Open Source Autopilot, http://ardupilot.org/

[20] Paz, M. and Leigh, W., "Integrated Matrix Analysis of Structures," Boston, MA: Springer US, 2001

[21] Skopinski, T.H., Aiken, W.S., Huston, W.B., "Calibration of Strain-Gage Installations in Aircraft Structures for the Measurement of Flight Loads," Technical Report NACA-TR-1178, National Advisory Committee for Aeronautics. Langley Aeronautical Lab, Langley Field, VA, 1954

[22] Preisighe Viana, M.V., "Sensor calibration for calculation of loads on a flexible aircraft," In: 16th International Forum on Aeroelasticity and Structural Dynamics, Saint Petersburg, Russia, 2015